

Late growth of early-type galaxies in low- z massive clusters

A. L. B. Ribeiro,¹★ R. S. Nascimento,² D. F. Morell,³ P. A. A. Lopes,⁴ C. C. Dantas⁵ and M. H. S. Fonseca^{1,4}

¹Laboratório de Astrofísica Teórica e Observacional, Universidade Estadual de Santa Cruz, Ilhéus, BA 454650-000, Brazil

²Laboratório Nacional de Astrofísica/MCTI, Itajubá 37504-364, Brazil

³Observatório Nacional, Rio de Janeiro, RJ 20921-400, Brazil

⁴Observatório do Valongo, Universidade Federal do Rio de Janeiro, RJ 20080-090, Brazil

⁵Instituto Nacional de Pesquisas Espaciais/MCTI, SP 12227-010, Brazil

Accepted 2023 February 6. Received 2023 January 16; in original form 2022 August 10

ABSTRACT

We study a sample of 936 early-type galaxies (ETGs) located in 48 low- z regular galaxy clusters with $M_{200} \geq 10^{14} M_{\odot}$ at $z < 0.1$. We examine variations in the concentration index, radius, and colour gradient of ETGs as a function of their stellar mass and loci in the projected phase space (PPS) of the clusters. We aim to understand the environmental influence on the growth of ETGs according to the time since infall into their host clusters. Our analysis indicates a significant change in the behaviour of the concentration index C and colour gradient around $M_{*} \approx 2 \times 10^{11} M_{\odot} \equiv \tilde{M}_{*}$. Objects less massive than \tilde{M}_{*} present a slight growth of C with M_{*} , with negative and approximately constant colour gradients in all regions of the PPS. Objects more massive than \tilde{M}_{*} present a slight decrease of C with M_{*} , with colour gradients becoming less negative and approaching zero. We also find that objects more massive than \tilde{M}_{*} , in all PPS regions, have smaller R_{90} for a given R_{50} , suggesting a smaller external growth in these objects or even a shrinkage possibly due to tidal stripping. Finally, we estimate different dark matter fractions for galaxies in different regions of the PPS, with the ancient satellites having the largest fractions, $f_{DM} \approx 65$ per cent. These results favour a scenario where cluster ETGs experience environmental influence the longer they remain and the deeper into the gravitational potential they lie, indicating a combination of tidal stripping + harassment, which predominate during infall, followed by mergers + feedback effects affecting the late growth of ancient satellites and BCGs.

Key words: galaxies: interactions – galaxies: structure – galaxies: statistics.

1 INTRODUCTION

Local early-type galaxies (ETGs) encompass objects that normally ceased their star formation, have red colours, small amounts of cold gas, and dust, and which correspond morphologically to ellipticals and lenticulars (e.g. Kauffmann et al. 2004; Blanton & Moustakas 2009). Some studies indicate that the formation of massive ETGs has occurred in two phases (e.g. Oser et al. 2010). At an early stage, the gas collapses into dark matter haloes and forms stars intensely for a short time interval (e.g. Thomas et al. 2005; Peng et al. 2010; Conroy, van Dokkum & Kravtsov 2015). The second phase involves mass accumulation through a series of mergers (e.g. Naab, Johansson & Ostriker 2009; Feldmann, Carollo & Mayer 2011; Johansson, Naab & Ostriker 2012; Huang et al. 2016) that enrich galaxies with stars set *ex situ*. In the Λ CDM cosmology, structures form hierarchically, with massive systems forming through the addition of less massive objects. It means that massive galaxies may have accreted large fractions of their current mass, with the accreted components deposited mainly in its outermost parts. On the contrary, low-mass galaxies are mostly made of stars formed *in situ* (e.g. Rodriguez-Gomez et al. 2016; Pillepich et al. 2018).

The two-phase formation scenario is consistent with the observations of quiescent galaxies at high redshifts ($z \sim 2$) that are very massive ($\sim 10^{11} M_{\odot}$) and compact ($R_e \sim 1$ kpc), usually called red nuggets (e.g. Van Dokkum et al. 2008; Damjanov et al. 2009; Newman et al. 2010; Whitaker et al. 2012). These objects are a factor of 2–4 times smaller than current ellipticals (e.g. Daddi et al. 2005; Trujillo et al. 2007; Van Dokkum et al. 2008), and there is evidence that they grow rapidly in size with little or no star formation (e.g. Van Dokkum & Conroy 2010; Damjanov et al. 2011; van der Wel et al. 2014; Buitrago et al. 2017). It means that whatever the growth process, it has the restriction to increase considerably the size of galaxies without significantly increasing their star formation rate. Indeed, the pre-dominance of old stellar populations in nearby massive ETGs is inconsistent with large episodes of recent star formation, which suggests that the mergers that form them either occurred very long ago (at redshifts $z > 2$), or they correspond to the coalescence of pre-existing old stellar populations (Thomas et al. 2005; Renzini 2006; Graves, Faber & Schiavon 2009), suggesting that dry mergers could explain the growth of these objects (e.g. Naab et al. 2009; Trujillo, Ferreras & de La Rosa 2011; Iodice et al. 2017; Mancillas et al. 2019). However, since merging processes are relatively rare in rich clusters due to their high velocity dispersions, the late growth of ETGs must originate from a combination of other environmental mechanisms, such as tidal stripping, galaxy harassment, and dynamical friction around central galaxies (e.g.

* E-mail: albr@uesc.br

Boselli & Gavazzi 2006; Cimatti, Fraternali & Nipoti 2019). Galaxies can also experience significant pre-processing in filaments and groups before infalling into massive clusters (e.g. Kuchner et al. 2022).

Some studies indicate that the environment plays an important role in this late evolution of galaxies. For instance, Shankar et al. (2013) suggest that many compact ETGs at high redshifts have evolved into the ETGs observed in high-density environments in the Local Universe. Lani et al. (2013) show that there is a strong relationship between the size of quiescent galaxies and the environment where they are located, such that massive objects ($M_* \geq 10^{11} M_\odot$) are significantly larger in high-density environments. However, Cypriano et al. (2006) find evidence for the shrinking of cluster ellipticals at $z < 0.08$, probably via tidal stripping, which is consistent with the result of Matharu et al. (2019), indicating that the disappearance of the compact cluster galaxies might be explained if, on average, ~ 40 per cent of them merge with their brightest cluster galaxies (BCGs) and ~ 60 per cent are tidally destroyed into the intracluster light between $0 \leq z \leq 1$. Also, Oogi, Habe & Ishiyama (2016) use numerical simulations to investigate the role of dry mergers in the evolution of the mass–size relationship of ETGs in massive haloes and find that central galaxies in low- z clusters with $M \sim 10^{14} M_\odot$ are potential descendants of the red nuggets observed in $z \sim 2$ –3. Yoon, Im & Kim (2017) find that local ETGs heavier than $10^{11.2} M_\odot$ show a clear environmental dependence in mass–size relation, in such a way that galaxies are as much as 20–40 per cent larger in the densest environments than in underdense environments. On the other hand, some studies do not indicate a correlation between the environment and the size growth of galaxies (e.g. Allen et al. 2015; Damjanov et al. 2015; Saracco et al. 2017).

An important point about studying galaxies in clusters is that once inside these systems, the galaxies remain there, allowing to connect high redshift and local objects without needing to appeal to abundance matching to link populations at different epochs (Guo et al. 2010; De Propriis, Bremer & Phillipps 2016; Wellons & Torrey 2017). Another point to be considered is that the dynamics of galaxy clusters is closely associated with the orbits of member galaxies. Different Hubble types are usually related to different orbits, with ETGs presenting more isotropic orbits than late-type galaxies (e.g. Biviano et al. 2002; Aguerri, Sánchez-Janssen & Muñoz-Tuñón 2007; Cava et al. 2017; Mamon et al. 2019). At the same time, E and S0 galaxies show smaller velocity dispersions than spirals and irregulars (e.g. Sodre et al. 1989; Stein, Jerjen & Federspiel 1997; Adami et al. 1998b; Biviano et al. 2002). Also, Nascimento et al. (2019) find that the passive population in systems with Gaussian velocity distribution is the only family with lower velocity dispersion in massive clusters. Morell et al. (2020) find a similar result showing that ellipticals and lenticulars have the most isotropic orbits.

These examples of morphological and orbital segregation suggest that ETGs are former entrants into the potential of clusters. However, the constant infall of galaxies into clusters can produce a mixture between ancient and recent early-type objects. According to Berrier et al. (2008), the accretion times for $z = 0$ cluster members are quite extended, with ~ 20 per cent incorporated into the cluster halo more than 7 Gyr ago and ~ 20 per cent within the last 2 Gyr. The effect of infalling objects can be studied using the distribution of the projected positions and velocities of cluster galaxies, due to the relationship between the region in the projected phase space (PPS) and the time since infall of objects, as shown by the recent works of Rhee et al. (2017, 2020), Pasquali et al. (2019), Sampaio et al. (2021), and de los Rios et al. (2021). This connection makes galaxy clusters good laboratories to study environmental effects on the growth of

ETGs, since we can define galaxy samples that inhabit the systems for different time-scales.

In this work, we study the concentration index, radius, dark matter fraction, and colour gradient of ETGs as a function of stellar mass and PPS regions in regular massive clusters ($M_{200} \geq 10^{14} M_\odot$) at low redshifts. Since most of the growth of ETGs happened at $z \gtrsim 0.3$ (López-Sanjuan et al. 2012; Ownsworth et al. 2014), we aim to understand the environmental influence on the late growth of ETGs according to the time since infall into their host clusters. The paper is structured as follows: In Section 2, we present the data. The analysis is presented in Section 3. In Section 4, we give a summary of the results and our conclusions. Throughout this paper, we adopt the cosmology with $\Omega_m = 0.3$, $\Omega_\Lambda = 0.7$, and $H_0 = 100 h \text{ km}^{-1} \text{ s}^{-1} \text{ Mpc}^{-1}$, with h set to 0.7.

2 DATA

Our sample was obtained from the extended version of Friends-of-Friends (FoF) group catalog originally identified by Berlind et al. (2006) and contains 5352 groups with $N > 5$ and $0.03 \leq z \leq 0.11$, consisting of galaxies with absolute magnitudes $M_r \leq -20.5$, and stellar masses in the range $10.4 < \log(M_*/M_\odot) < 11.9$,¹ with median $\sim 10^{11} M_\odot$. This version is described in La Barbera et al. (2010) and differs from the first one only in the area used (9380 square degrees from SDSS-DR7, compared to the original area of 3495 square degrees from the DR3). We derived a refined central redshift by applying the gap technique (Adami et al. 1998a; Lopes 2007; Lopes et al. 2009) to the central (0.67 Mpc) galaxies. We also obtained a member list for each group using the ‘shifting gapper’ technique (Fadda et al. 1996; Lopes et al. 2009), extending to ~ 4 Mpc around the group centres defined by La Barbera et al. (2010). The groups were then subject to the virial analysis, analogous to that described in Girardi et al. (1998), Popesso et al. (2005, 2007), Biviano et al. (2006), and Lopes et al. (2009). This procedure yields estimates of velocity dispersion (σ_v), radii (R_{500} , R_{200}), and masses (M_{500} , M_{200}) for most of the groups from the FoF sample. In the present work, we studied a subsample containing 107 massive clusters, with at least 20 galaxies within R_{200} , implying systems with $M_{200} \gtrsim 10^{14} M_\odot$ extending to $2R_{200}$.

We added to the resulting sample the stellar masses from the *galSpecExtra* table (Kauffmann et al. 2004), corresponding to the *lgm_tot_p50* parameter. We also used the Domínguez Sánchez et al. (2018) catalog, which provides morphological T types for $\sim 670\,000$ galaxies from SDSS, by training convolutional neural networks with information from available sources such as Galaxy Zoo 2 (GZ2; Lintott et al. 2008; Willett et al. 2013) and the catalog of visual classifications provided by Nair & Abraham (2010), from which we included the probabilities of galaxies having a dominant bulge (P_{bulge}) and being S0 (P_{S0}). Our sample was also cross-matched with Korean Institute for Advanced Study Value-Added Galaxy Catalog (Park & Choi 2005), which provides some relevant photometric information, such as the rest-frame colour gradient $\Delta(g - i)$ and the concentration index $C = R_{90}/R_{50}$. Finally, we added the Sérsic indices n in the r -band from the catalog of Simard et al. (2011).

We defined a sample of 936 ETGs as objects with $T < 0$, $P_{bulge} > 0.5$ and $n > 2.5$ located in 48 clusters without substructures, according to the Dressler-Schectman (DS) test (Dressler & Schectman 1988); and with Gaussian velocity distribution, according to the Hellinger Distance (HD) metric (see Ribeiro et al. 2013; de Carvalho

¹We use the notation ‘log x ’ as indicating the decimal logarithm of x .

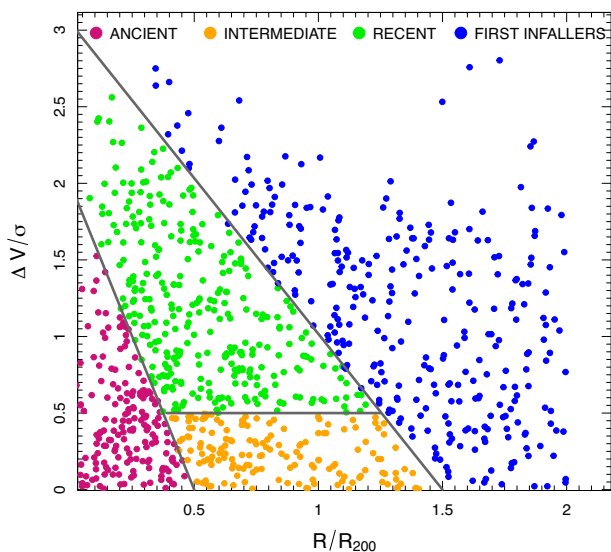


Figure 1. Distributions of ETGs in different PPS regions. Ancients objects are in red, intermediate in orange, recent in green, and the first infallers are in blue.

et al. 2017). Both DS and HD indicators were used at the 90 per cent confidence level², which means we restrict our study to systems likely to be virialized, avoiding the dynamical effects of interacting clusters and possible deviations from the expected homology of galaxy systems.

Galaxies are studied according to their loci in the PPS, which is built by normalizing the projected clustercentric distances and velocities by the virial radius, R_{200} , and velocity dispersion, σ_v , respectively. To explore the PPS, we divide cluster galaxies into four subsamples, following the classification introduced by Rhee et al. (2017): ancient infallers (region E in their fig. 6), recent infallers (regions B & C), intermediate infallers (region D), and first infallers (region A). These regions are related to the time since infall (t_{inf}) in Gyr:

- 1) Ancient $\rightarrow 6.5 \lesssim t_{inf} \lesssim 13.7$
- 2) Intermediate $\rightarrow 3.6 \lesssim t_{inf} \lesssim 6.5$
- 3) Recent $\rightarrow 0 < t_{inf} \lesssim 3.63$
- 4) First infallers \rightarrow objects which are not completely fallen yet

In Fig. 1, we present the distribution of ETG galaxies in the PPS regions of Rhee et al. (2017), following the approximation of Song et al. (2018). All the ancient (171 objects), intermediate (157 objects), recent (307 objects), and first infallers (301 objects) are shown in this figure.

3 ANALYSIS

In the following, we compare some properties of ETGs in the PPS samples, also comparing them to a sample of isolated ETGs taken from the list of one-member groups of the catalog of Yang et al. (2007). This field sample, composed of 6670 objects, is defined with the same criteria (except membership) used to select the cluster ETGs.

²The HD metric is not a statistical test, so its confidence level must be understood as a confiability derived from bootstrap realizations, as described in de Carvalho et al. (2017).

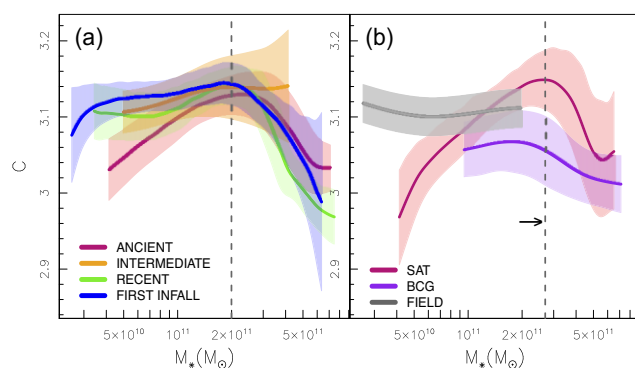


Figure 2. Stellar mass–concentration plane of ETGs selected in the four PPS regions. (a) Ancients objects are in red, intermediate in orange, recent in green, and the first infallers are in blue. (b) Satellites are in red, BCGs are in purple, and field galaxies are in grey. The dashed vertical lines indicate the behaviour change around $2 \times 10^{11} M_{\odot}$. Solid lines represent medians, while shaded areas show the confidence intervals calculated from 1000 bootstrap realizations.

3.1 Concentration index

A direct way to study the late growth of ETGs is to consider them in the cluster environment and compare their behaviour in the stellar mass–concentration plane, taking into account their positions in the PPS, which is our basic aim in this work. The concentration index reflects the current light distribution concerning R_{50} and R_{90} , which can be affected in different ways by the environment. Examining the concentration index as a function of the stellar mass, we find a significant change in the behaviour of C around $M_* \approx 2 \times 10^{11} M_{\odot} \equiv \tilde{M}_*$, see panel (a) in Fig. 2. Objects less massive than \tilde{M}_* present a slight growth of C with M_* , while more massive objects present an opposite trend, except for those in the intermediate region.³

To better understand this result, we separated the sample of ancients, building a subsample of the BCGs and another of satellites (SAT). The subsample of BCGs is composed of the 48 most luminous ancient cluster ETGs (each taken from a cluster) having $M_r < -21.4$ and $M_* > 10^{11} M_{\odot}$; and the SAT subsample is composed of the other 123 ancient galaxies. The behaviour of these subsamples is shown in panel (b) of Fig. 2. The behaviour of SATs is the same (just slightly accentuated) as that of the total ancient sample, while BCGs have a narrower mass range (with no objects with $M_* < 10^{11} M_{\odot}$) and lower values of C than SATs and field galaxies. We also should note that BCGs have a slightly decreasing behaviour, while the curve of field galaxies is approximately flat. The flatter behaviour of the field sample suggests an environmental effect on the light distribution of cluster ETGs. For objects less massive than \tilde{M}_* , the PPS samples (especially the ancients) present a slightly higher growth (or a minor shrinkage) of R_{90} with respect to R_{50} (except for BCGs), and an opposite behaviour for objects with $M_* > \tilde{M}_*$.

According to Rhee et al. (2017), there is a direct correlation between time since infall and tidal mass-loss in the sense that objects longer in clusters have experienced a higher rate of tidal mass loss. A similar result is found by Joshi, Wadsley & Parker (2017). Theoretically, tidal stripping from the cluster potential tends to preferentially affect the outer galaxy first, causing an outside-in stripping (see

³The intermediate region presents a small number of very massive galaxies (only 12 objects), a point to be discussed later. Also in this figure, we show the behaviour of field galaxies.

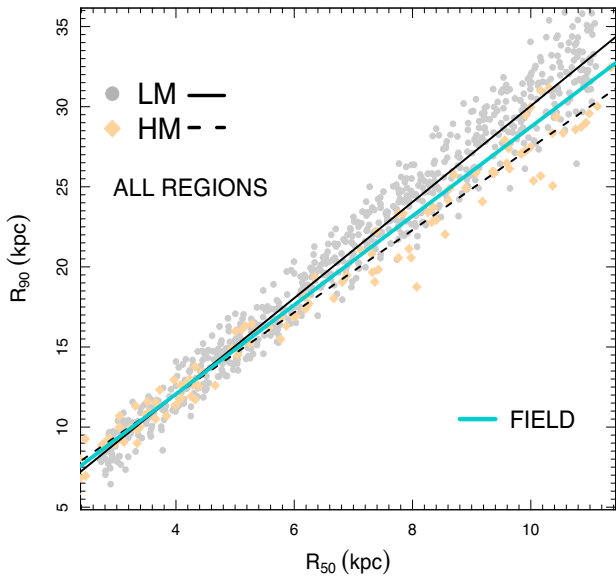


Figure 3. Regression lines for the $R_{50} \times R_{90}$ relations of LM and HM ETGs taken from all PPS regions. Grey circles indicate LM objects and beige diamonds indicate HM objects. The solid black line depicts LM ETGs, while the dashed black line depicts HM ETGs. The solid cyan line is the regression line of the field ETGs.

Binney & Tremaine 1987). Similarly, tidal stripping from impulsive galaxy–galaxy encounters (the harassment) preferentially affects the outer galaxy first (see Smith et al. 2016). In addition, Łokas (2020) shows that, as a result of tidal stripping, galaxies weakly evolved (those with one pericentric passage) lose between 10 per cent and 80 per cent of their dark mass and less than 10 per cent of stars, while objects strongly evolved (those with multiple pericentric passages) lose more than 70 per cent of dark mass and between 10 per cent and 55 per cent of stellar mass. All this suggests an effect on the light distribution of galaxies in their outermost parts, possibly implying a shrinkage of R_{90} at different rates, being higher for objects more massive than \bar{M}_* and lower for less massive objects. Running robust linear regressions between R_{50} and R_{90} for objects more or less massive than \bar{M}_* [high mass (HM) and low mass (LM), respectively], we see that the relationship for LM objects is steeper – see Fig. 3. Also, in this figure, field ETGs present an intermediate slope.⁴ To test the difference between slopes, we use the analysis of variance (ANOVA) and find that the slopes $\beta_{LM} = 3.03 \pm 0.06$, $\beta_{HM} = 2.69 \pm 0.08$, and $\beta_{FIELD} = 2.78 \pm 0.04$ are significantly different at the 90 per cent confidence level. The different slopes imply small but significant differences between the median concentration indices for LM ($C = 3.13 \pm 0.03$) and HM ($C = 3.03 \pm 0.05$) objects in all PPS regions.

The results of this section and the next ones may be subject to two types of contaminants: (i) objects misclassified as cluster members and (ii) contaminants with respect to the boundaries of the regions defined by Rhee et al. (2017). The first type of contaminants will be disregarded in this work since our shift gapper + virial analysis code has been compared to a set of 24 galaxy-based cluster mass estimation techniques and proved to be among the best three (Old et al. 2015), so the number of intruder galaxies remaining after applying the method should not be significant. The second type of contaminant is due to projection effects, i.e. the properties of galaxies

⁴We have not included the points of field ETGs so as not to saturate the figure.

identified in 3D differ from their properties when they are identified on the PPS (e.g. Coenda et al. 2022). Indeed, Rhee et al. (2017) quantify the probability that a galaxy in a particular location belongs to a particular infall region, and they also quantify the 1σ error on this probability due to cluster-to-cluster variations, and differing lines of sight. To consider this, we assume the same contamination fractions in each region of the PPS as given by Rhee et al. (2017; see their fig. 6). For each reference region, we randomly select points from the other three regions, according to the contamination fractions, and reclassify the selected data points to the given reference region. After repeating the procedure 100 times, we check the variation of galaxy categorizations. The procedure allows checking how many galaxies were misclassified in a given class and by which of the other classes. According to Rhee et al. (2017), the overall highest numbers of contaminants come from the recent class, which significantly contaminates the others, especially the ancient class. Indeed, mutual contamination between all regions appears in varying degrees. Still, our tests indicate that these unavoidable misclassifications, even in noteworthy cases such as the recent class contaminants, do not lead to significant changes in the trends since they do not imply variations that exceed the confidence intervals in all studied bins. (see Appendix A). Another point possibly affecting our results is the different stellar mass intervals of the samples, as one can see in Fig. 2. But running the analysis in the approximate same range of stellar mass, $10.6 \lesssim \log(M_*/M_\odot) \lesssim 11.4$, building subsamples of 857 (cluster) and 5821 (field) galaxies, we find that the results are approximately the same. From now on, all average properties of ETGs will be obtained for these reduced samples.

To further explore the structural evolution of cluster ETGs, in the following subsection, we study the behaviour of R_{50} and R_{90} according to the PPS regions.

3.2 Growing (or not) in size

The results presented so far suggest a differentiated growth (or shrinkage) of ETGs as a function of their stellar mass. Now we analyse what happens to the radii R_{50} and R_{90} according to the PPS regions. First, we study the variation of R_{90} after the galaxy enters the cluster. As previously discussed, R_{90} is expected to be affected by tidal stripping and harassment during galaxy infall. Fig. 4 shows the evolution of this radius from the field to BCGs. Note that the first stages of infall do not significantly change R_{90} , until the first pericentric passage occurs, causing a remarkable shrinkage of the galaxies. However, after multiple pericentric passages, galaxies grow in size again, reaching values of $R_{90} \sim 1.5$ times larger than they had just after the first pericentric passage. This increase in size for ancient objects can be explained by the occurrence of mergers and/or feedback processes. Mergers can increase the size of galaxies but usually also raise the Sérsic index to $n > 5$ (e.g. Hilz, Naab & Ostriker 2013). Although mergers are not frequent in massive clusters, dynamical friction acting on central galaxies can reduce velocities and increase the rate of mergers and cannibalism on more massive objects (e.g. Chandrasekhar 1943; Goto 2005; Nipoti 2017; Tamfal et al. 2021). In addition, objects that lose mass during the first pericentric passage can undergo dynamical self-friction, the process by which material that is stripped from a subhalo torques its remaining bound remnant, which causes it to lose orbital angular momentum and favours mergers (Miller et al. 2020).

On the other hand, Smith et al. (2016) find that feedback effects, such as galactic winds or displacement of black holes from the centre of galaxies, can lead to an increase in size (via adiabatic expansion) but not in the shape of central galaxies. In Fig. 5, we see the relation

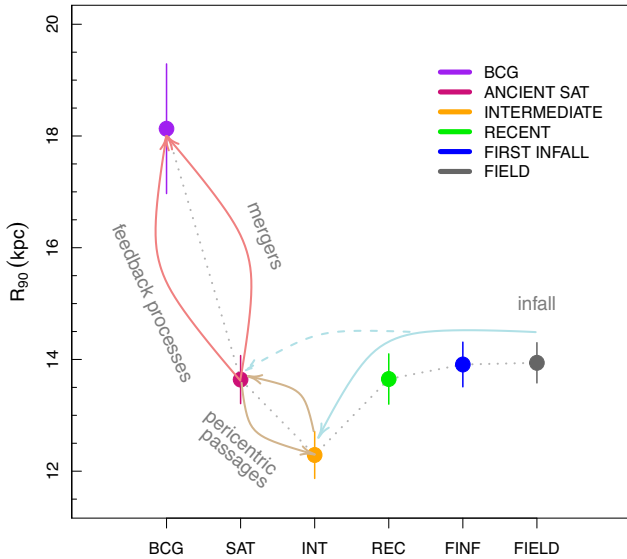


Figure 4. Evolution of R_{90} (in kpc) across the PPS regions. Points and error bars indicate median values and bootstrap errors for 1000 resamplings. Ancients satellites are in red, intermediate in orange, recent in green, first infallers in blue, BCGs in purple, and field galaxies are in grey. Light blue arrows indicate the infall; orange arrows indicate the pericentric passages; and red arrows indicate processes leading to the formation of the giant central ETGs.

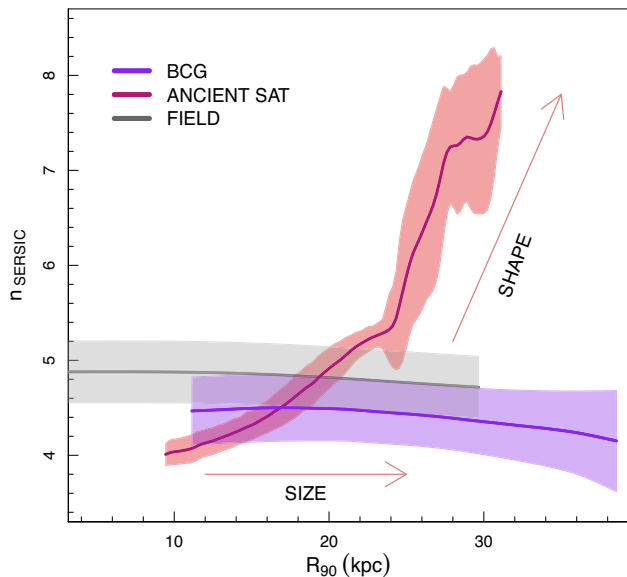


Figure 5. Relation between size given by R_{90} and shape given by the Sérsic index n . Red lines for ancient satellites, purple for BCGs, and grey for field ETGs.

between R_{90} and the Sérsic index n for ancient objects (satellites and BCGs) and field galaxies, as a comparison. Note in this figure that field galaxies and BCGs vary significantly in size but not in shape. At the same time, ancient satellites grow in both R_{90} and n , with the Sérsic index reaching $n \approx 8$, which could be obtained after two intermediate (mass ratio 1:5) dry mergers (Smith et al. 2016). This result indicates that BCGs grow preferentially via feedback mechanisms, in agreement with Ascaso et al. (2010) that explain the increase in size and the non-evolution in the Sérsic shape parameter of the BCGs in the last 6 Gyr through feedback processes. Alternatively,

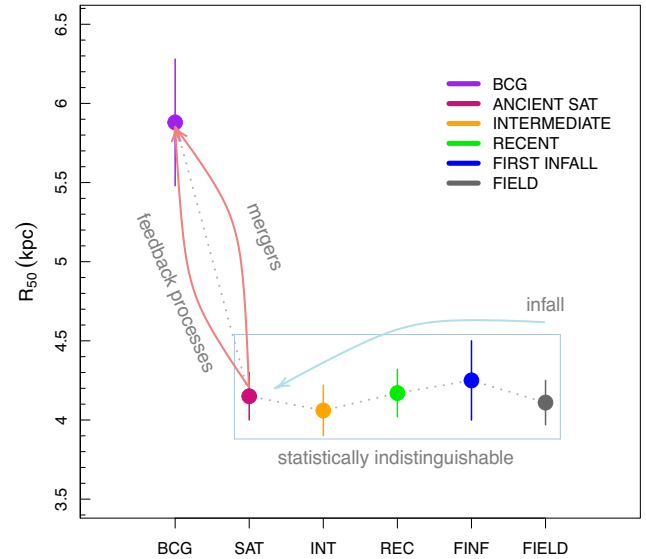


Figure 6. Evolution of R_{50} (in kpc) across the PPS regions. Points and error bars indicate median values and bootstrap errors for 1000 resamplings. Ancients satellites are in red, intermediate in orange, recent in green, first infallers in blue, BCGs in purple, and field galaxies are in grey. Light blue arrows indicate the infall; orange arrows indicate the pericentric passages; and red arrows indicate processes leading to the formation of the giant central ETGs.

BCGs may also have reached their final size in earlier stages of cluster formation. Assuming that part of the ancient satellites can merge with BCGs, the result indicates that the latter can grow via both mechanisms.

To complete the analysis, we finally show how R_{50} varies according to the PPS regions. In Fig. 6, we see that the values of R_{50} do not change significantly during the infall, indicating that environmental effects do not change the light distribution at this scale. However, for ancient objects, we notice a remarkable growth in size up to the BCG values.

3.3 Colour gradient

Several studies show that local ETGs have negative colour gradients, indicating that their stellar populations become bluer towards the galaxy outskirts (e.g. Peletier et al. 1990; La Barbera & De Carvalho 2009; Gargiulo et al. 2012). This behaviour also supports the scenario where ETGs assemble most of their stellar mass at high redshifts ($z \gtrsim 2$), and then experience passive evolution interspersed by dry minor mergers over cosmic time (e.g. Di Matteo et al. 2009; Hilz et al. 2013). The study of ETGs through the PPS regions of clusters (i.e. their time evolution within a dense environment) can help us to better understand the late environmental effects on ETGs. In this work, the rest-frame colour gradient $\Delta(g - i)$ is defined as the difference in colour of the region with $R < R_{pet}$ from that of the annulus with $0.5R_{pet} < R < R_{pet}$, where R_{pet} is the Petrosian radius. According to this definition, a negative colour difference means a bluer outside (or redder centres; Park & Choi 2005).

In Fig. 7, we see how colour gradients $\Delta(g - i)$ vary with the stellar mass of the ETGs. The first point to note in panel (a) of this figure is a change in the general behaviour at approximately the same mass where we observe a transition in the concentration index, \tilde{M}_* . For lower masses, colour gradients are negative and approximately constant in all samples, while for $M_* > \tilde{M}_*$, colour gradients tend to

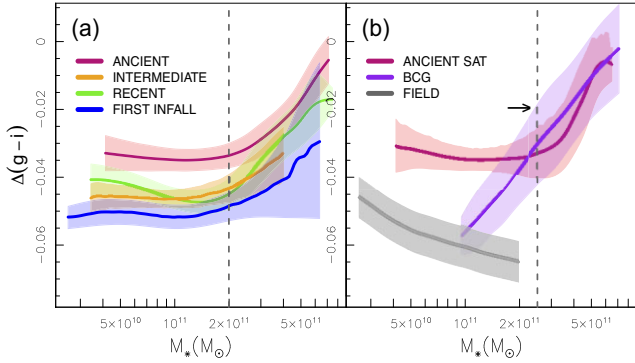


Figure 7. Colour gradient dependence on the stellar mass of ETGs selected in the four PPS regions. Ancients objects are in red, intermediate in orange, recent in green, and the first infallers are in blue. The dashed vertical line indicates the behaviour change around \tilde{M}_* . Solid lines represent medians, while shaded areas show the confidence intervals calculated from 1000 bootstrap realizations.

become less negative with M_* . Two-sample permutation comparisons indicate (at the 95 per cent C.L.) that the ancient population has the most positive colour gradients (-0.034 ± 0.004), while the recent + intermediate samples have in-between values (-0.045 ± 0.004), and the first infallers are the ones with the most negative colour gradients (-0.051 ± 0.003). This result points to objects longer in the clusters having less negative colour gradients. At the same time, more massive objects show an increasing trend of the colour gradient with M_* in all PPS regions. Usually, the centres of ETGs are older and more metal-enriched than their outskirts, producing negative colour gradients. To make them less negative, the action of tidal stripping would be removing the outskirts and/or dry mergers would be flattening the colour gradients. According to the relationship between infall time and tidal stripping, ETGs with a stellar mass smaller than \tilde{M}_* present a small shrinkage of R_{90} (or smaller sizes with respect to R_{50} – as we found in the previous sections), indicating that tidal stripping could explain the behaviour of colour gradients for these objects. It is important to note that this behaviour does not change with stellar mass, as opposed to what happens with more massive objects, as we can see in panel (b) of Fig. 7, for which the colour gradients increase almost linearly with stellar mass, indicating that mergers may affect these objects by reducing (approaching zero) the mean colour gradients. The flattening can also be favoured by pre-processing, where more massive objects can pass through mergers in groups before entering the clusters. As for field objects, low-mass ETGs have colour gradients similar to those of first infallers. The values become more negative for objects with higher stellar masses, possibly indicating the absence of mechanisms pruning the blue edges of these objects.

3.4 $M_*-\sigma$ relation

The scaling between stellar mass and velocity dispersion is one of the fundamental connections observed in ETGs (e.g. Shen et al. 2003; Hyde & Bernardi 2009; Roy et al. 2018; Tortora et al. 2018; Zahid, Sohn & Geller 2018), and it directly follows the Faber–Jackson relationship (Faber & Jackson 1976). Stellar velocity dispersion depends on the gravitational potential and therefore relates galaxies to their dark matter haloes (e.g. Evrard et al. 2008; Schechter 2016). At the same time, the stellar mass indicates the amount of baryonic mass converted into stars. Zahid et al. (2018) use data from the Illustris simulations to show that the stellar velocity dispersion is

equal to the velocity dispersion in the dark matter halo. The observed relationship follows $\sigma \propto M_*^{0.3}$ for $M_* > 10^{10.3} M_\odot$ (e.g. Cappellari 2016; Zahid et al. 2016), which is approximately the same relation between σ_{DM} and M_{200} for dark matter particles (Zahid et al. 2018). Although the $M_*-\sigma$ relation does not show significant evolution at $z < 0.7$ (Zahid et al. 2016), environmental effects may be affecting the relation for clusters ETGs with $M_* > 10^{11.2} M_\odot$, since these objects experience major and minor mergers more frequently in high-density environments (Yoon et al. 2017). Indeed, the results presented in the previous sections indicate that dynamical friction may slow down ancient satellites that vary greatly in size and shape, suggesting mergers in clusters or possibly in infalling groups where pre-processing took place. On the other hand, less massive ETGs seem to be affected by tidal stripping in the cluster environment.

We study the behaviour between M_* and σ for galaxies in the PPS subsamples. The central stellar velocity dispersions are aperture corrected by the equation of Cappellari et al. (2006):

$$\sigma = \sigma_{\text{fiber}} \left(\frac{8r_{\text{fiber}}}{R_e} \right)^{0.066} \quad (1)$$

where σ_{fiber} is the estimated velocity dispersion in SDSS, R_e is effective or the angular half-light radius in arcsec, and r_{fiber} is the radius of SDSS fibers, 1.5 arcsec. We only use ETGs with $100 < \sigma < 420 \text{ km s}^{-1}$ since values below 100 km s^{-1} are unreliable (e.g. Bernardi et al. 2003), and SDSS uses template spectra convolved to a maximum velocity dispersion of 420 km s^{-1} (see e.g. Yoon & Park 2020). The effective radii are calculated by

$$R_e = a_{\text{dev}} \sqrt{b/a} \quad (2)$$

where a_{dev} and b/a are the semimajor axis length and the axis ratio from the de Vaucouleurs fit, respectively. We only use ETGs with $b/a > 0.3$ to avoid edge-on objects. The restrictions on σ and b/a reduce the sample to 912 galaxies. The parameters a_{dev} , b/a , and σ_{fiber} in r -band are taken from the catalogs PhotObjAll and SpecObjAll of DR15 (Aguado et al. 2019).

In Fig. 8, we see all the robust linear regressions between central velocity dispersion and stellar mass of ETGs in the PPS regions (separating the ancients into BCGs and satellites) plus the field ETGs. Using ANOVA to compare the slopes from each sample, we find that most of the samples present a similar slope, $\beta \approx 0.3$, except with respect to the ancient objects, for which we find $\beta = 0.45 \pm 0.07$ for the satellites, and $\beta = 0.18 \pm 0.08$ for the BCGs, statistically distinct values at the 95 per cent confidence level.

The slopes indicate how much change there is in the central velocity dispersion when the stellar mass changes, with slopes significantly above or below ≈ 0.3 , indicating a higher or lower fraction of dark matter in galaxies. Zahid et al. (2018) showed that the central stellar velocity dispersion of quiescent galaxies is proportional to the dark matter halo velocity dispersion. Therefore, our results indicate an increase of dark matter in ancient satellites and a deficit in BCGs. This is consistent with what we find in the previous sections, i.e. satellites in the central region of clusters are probably going through mergers (see e.g. Fig. 5). Although mergers do not occur in clusters with high rates at low- z , there are several observational evidence for dry merging at $z < 0.3$ in central galaxies of groups and clusters (e.g. McIntosh et al. 2008; Liu et al. 2009; Rasmussen et al. 2010; Edwards & Patton 2012). In particular, Liu et al. (2015) have obtained a major dry merger rate of 0.55 ± 0.27 merger per Gyr at $z \sim 0.43$. Even such a low merger rate can promote the growth of dark matter haloes in ancient ETGs since they have time since infall ≥ 6.5 Gyr. On the other hand, the constancy of the Sérsic index does not indicate significant mergers for the BCGs,

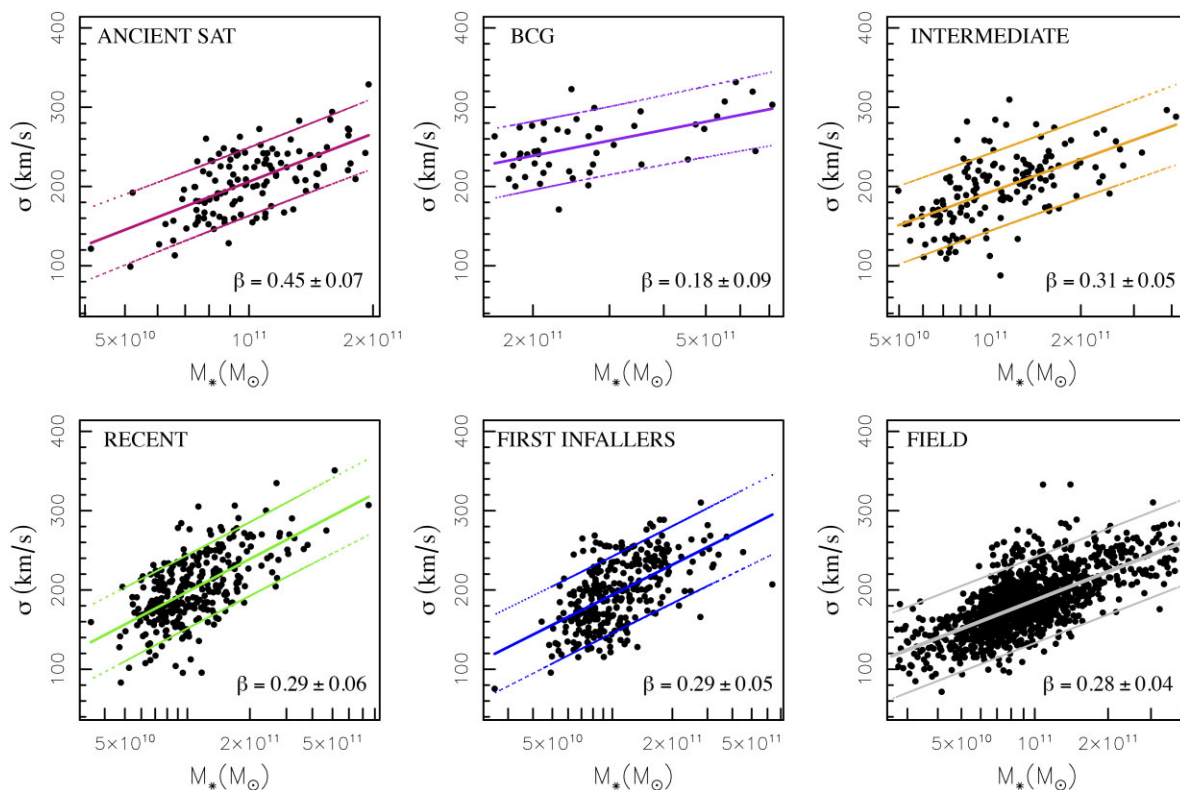


Figure 8. Stellar mass versus central velocity dispersion of ETGs selected in the four PPS regions. Linear fits plus 1σ errors for ancient satellites are depicted in red lines, with BCGs in purple, intermediate in orange, recent in green, first infallers in blue, and field galaxies in grey lines.

and the shallower slope in the M_* – σ relation must be related to feedback mechanisms and/or to the fact that the BCGs could not constitute virialized configurations. The presence of self-interacting DM in haloes can also explain lower central DM densities by making the core radius larger (e.g. Rocha et al. 2013; Di Cintio et al. 2017). Lower DM fractions could also be associated with diffuse DM haloes (Alabi et al. 2017), or due to non-universal Initial Mass Function (IMF) and non-homology of ETGs (see e.g. Tortora & Napolitano 2022).

3.5 Difference between dynamical and stellar mass

Another way to explore the distribution of dark matter in ETGs through the PPS regions is to consider the difference between the dynamical (virial) mass and the stellar mass of galaxies. We can estimate the dynamical mass using the following expression:

$$M_{\text{dyn}} \simeq K(n) \frac{R_e \sigma^2}{G} \quad (3)$$

(see Poveda 1958; Nigoche-Netro et al. 2019), where $K(n)$ is a scale factor that depends on the Sérsic index n as follows

$$K(n) = 8.87 - 0.831n + 0.00241n^2 \quad (4)$$

(Cappellari et al. 2006), with the Sérsic indices taken from the catalog of Simard et al. (2011). We also define the ratio M_{dyn}/M_* as

$$\Delta M \equiv \log(M_{\text{dyn}}/M_\odot) - \log(M_*/M_\odot) \quad (5)$$

following the work of Nigoche-Netro et al. (2019). We present the cumulative distribution functions (CDFs) of ΔM for the PPS samples in Fig. 9 and use the Conover test to compare them against each other (Conover & Iman 1979). We use the version from the DESCtools

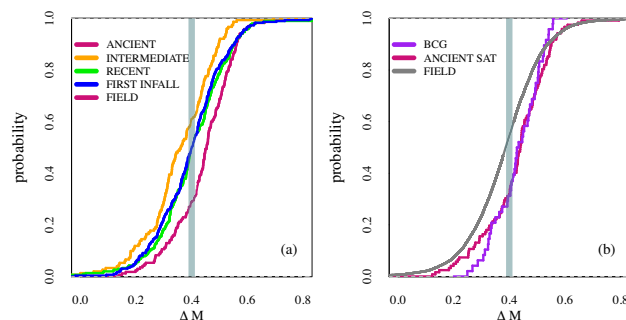


Figure 9. Cumulative distribution functions of the logarithmic difference between dynamical and stellar mass, ΔM . In panel (a), we show ancient objects in red, intermediate in orange, recent in green, and the first infallers in blue. In panel (b), we show BCGs in purple, ancient satellites in red, and field ETGs in grey. The shaded area in both panels indicates the range of median values of ΔM for the samples with $z < 0.12$ studied by Nigoche-Netro et al. (2019).

R package (Signorell et al. 2016). The test performs a multiple comparison between the data sets and verifies whether the CDF of one does not cross the CDF of the other at the 90 per cent C.L.⁵ The test indicates significant differences between ancient objects and all other samples, as well as intermediate objects and all others, not indicating a significant difference between recent, first infallers, and field ETGs. We also find no significant difference between the BCGs and the ancient satellites. In Fig. 9, we show the CDFs of the

⁵See a previous astrophysics application of this test in Morell et al. (2020).

logarithmic difference between dynamical and stellar mass for the PPS samples in panel (a), and BCG, SAT, and field samples in panel (b). The shaded areas in both panels indicate the range of median values of ΔM for the samples with $z < 0.12$ studied by Nigoche-Netro et al. (2019), [0.388, 0.411] for low- z ETGs. In comparison, our PPS samples have the following median values: 0.431 ± 0.015 (all ancient), 0.358 ± 0.028 (intermediate), 0.399 ± 0.013 (recent), and 0.398 ± 0.017 (first infallers). Separating the ancients: 0.421 ± 0.019 (BCGs) and 0.438 ± 0.016 (satellites), while the field ETGs present 0.389 ± 0.011 . The medians and respective errors are computed from 1000 bootstrapped resamplings. This result suggests that ancient ETGs have a higher fraction of dark matter, while intermediate objects have a lower fraction, with the recent, first infall, and field subsamples having values in the middle. Not only does this reinforce the idea of environmental effects on the distribution of dark matter in cluster ETGs, but it also gives us clues to understand the process taking into account their orbits and trajectories through the PPS of the clusters. In fact, the result seems to indicate that objects with an infall time $\lesssim 3.63$ Gyr are not significantly affected by dynamical processes that affect the dark matter fraction (f_{DM}), which remains at the level of ~ 60 per cent (after translating to linear scale), agreeing with the median f_{DM} found by Nigoche-Netro et al. (2019) for low- z samples. At the same time, ancient ETGs have a slight (but significant) increase in f_{DM} to 65 per cent, while intermediate ETGs have f_{DM} decreased to 56 per cent.

The decrease in f_{DM} during the intermediate phase could be the result that objects in this region had their first pericentric passage recently and may have lost part of their mass at this stage. Indeed, Gill, Knebe & Gibson (2005) report that cluster galaxies with low projected velocities, usually identified as backplash galaxies, lose a fraction of their mass in their first passage through the cluster core. Muriel & Coenda (2014) find that ETGs with very low projected velocities ($|\Delta V| < 0.5\sigma_{cl}$), where σ_{cl} is the velocity dispersion of the host cluster, are systematically less massive than ETGs at higher velocities. To compare, our intermediate population typically has $|\Delta V| \approx 0.25\sigma_{cl}$. In addition, Rhee et al. (2017) find a significant tidal mass-loss of dark matter after the first pericentre passage; a similar result is found by Joshi et al. (2017). Interestingly, our intermediate population presents a cut-off in stellar mass around $10^{11.6} M_{\odot}$, while the other populations reach $\sim 10^{11.9} M_{\odot}$. This reinforces the conclusion that ETGs in this region of the PPS have either lost part of their mass (both stellar and dark matter) and/or are unable to add mass through dynamical processes. Finally, we need to reconcile the higher f_{DM} in ancient ETGs with the DM deficiency obtained from the $M_{*}-\sigma$ relation for BCGs. It is well known that BCGs have larger R_e , at fixed stellar mass than the general early-type population and their velocity dispersion increases less with stellar mass (e.g. Bernardi 2009). From equations (1) and (3), we see that larger R_e decreases σ and increase M_{dyn} , which could partially explain the result. The increase in R_e can be associated with feedback effects and other effects we mentioned in the previous section. Understanding the physical processes driving the evolution of BCGs is essential for studying the formation history of galaxy clusters. Our analysis indicates early-type BCGs differ significantly from the general ETG population in low- z clusters. Still, a more specific study on the evolution of BCGs will be presented in a forthcoming paper.

4 DISCUSSION

The study of cluster ETGs is essential to improve our understanding of the structure formation and the galaxy–environment connection. Advances in this topic may allow us to understand how the environ-

ment may or may not favour the late evolution of ETGs. The size growth of ETGs is a long-term process that can last until the present. Andreon (2018) shows that the environment has been affecting the sizes of ETGs since at least $z \approx 2$. Merging seems to be the main contributor to the size evolution of ETGs at $z \lesssim 1$ (e.g. López-Sanjuan et al. 2012), with massive local galaxies assembling ~ 75 per cent of their total stellar mass at $0.3 < z < 3.0$ (Ownsworth et al. 2014), indicating the need for late growth of ETGs at $z < 0.3$. However, the growth in size and mass of cluster ETGs is disfavoured by tidal effects, apart from the fact that mergers are less efficient in massive clusters. In this context, a significant result is found by Rhee et al. (2017), showing a direct correlation between time since infall and tidal mass-loss, in the sense that objects longer in clusters have experienced a higher rate of tidal mass-loss. In addition, Matteuzzi et al. (2022) show that the evolution in size and mass of cluster ETGs is related to the acquisition of new galaxies by the clusters and the transformation of member galaxies located at large clustercentric distances at $z = 0.85$, which end up being massive satellite ETGs at $z = 0$. Also, Tran et al. (2008) study BCGs and their early-type companions at $z \sim 0.37$ as an example of late stellar assembly of massive cluster galaxies via major merging.

In the present work, we present a study of cluster ETGs distributed in PPS regions defined by Rhee et al. (2017) and Song et al. (2018). The samples containing the oldest objects (ancient and intermediate ETGs) have the time since infall $\gtrsim 3.6$ Gyr, which places their entry into the cluster at $z \gtrsim 0.32$. For the recent and first infallers ETGs, their time since infall is $\lesssim 3.6$ Gyr. Despite this difference in t_{inf} , all the cumulative galaxy changes, before and after the infall, are roughly called late (or residual) growth since we define all the ETGs using the same criteria. So the differences we find between the PPS regions are, in principle, thought as a result of environmental effects in the clusters.

A possible caveat to the whole analysis is that the sample of ETGs has 77 per cent of ellipticals (E) and only 23 per cent of lenticulars (S0). We separate E from S0 following Barchi et al. (2020), considering ellipticals all objects with $T < -2$, and lenticulars all those with $-2 \leq T < 0$ with $P_{S0} > 0.6$. Removing the S0, we reproduce all the results presented in the previous sections. But using only the S0, the results become statistically inconclusive. Another difficulty inherent to this work is associated with the mutual contamination of objects from different regions of the PPS, as discussed in Section 3.1 and Appendix A.

Despite these limitations, the present work achieves some significant results capable of shedding light on the problem of late growth of ETGs in galaxy clusters. Our main findings are:

(i) We find a significant change in the behaviour of the concentration index C around \tilde{M}_{*} , see Fig. 2. Objects less massive than this present a slight growth of C with M_{*} , while more massive objects present an opposite trend. The flatter behaviour of the field sample, especially regarding ancient satellites, suggests an environmental effect on the the light distribution of cluster ETGs.

(ii) HM objects in all PPS regions show less growth (or more shrinkage) of R_{90} concerning R_{50} than LM objects (Fig. 3), and the infall seems to decrease R_{90} and not affect R_{50} (see Figs 4 and 6). But in the transition from the intermediate to the ancient region, we find a remarkable increase of R_{90} and R_{50} .

(iii) We also find that field galaxies and BCGs vary significantly in size but not in shape, while ancient satellites grow in both R_{90} and n , with the Sérsic index reaching $n \approx 8$, indicating that BCGs grow preferentially via feedback mechanisms at low- z (or that they have already reached their final size in earlier stages of cluster formation),

while central satellites probably experience a growth stage via dry mergers.

(iv) For LM objects, colour gradients are negative and approximately constant in all samples, while for HM ETGs, colour gradients tend to become less negative with M_* . The ancient population has the most positive colour gradients (-0.034 ± 0.004), while the recent + intermediate samples have in-between values (-0.045 ± 0.004), and the first infallers are the ones with the most negative colour gradients (-0.051 ± 0.003). This result points to objects longer in the clusters having less negative colour gradients.

(v) From the study of the $M_*-\sigma$ relation, we find an increase of dark matter in ancient satellites and a deficit in BCGs, indicating mergers for satellites and feedback mechanisms (or a more complex structure plus previous evolution) for BCGs.

(vi) Estimating the dynamical mass of galaxies, we find that ancient ETGs have a higher fraction of dark matter, while intermediate objects have a lower fraction, with the recent and first infall samples having values in the middle.

(vii) Finally, results (v) and (vi) can be reconciled for BCGs if mechanisms capable of increasing R_e act on these objects.

These results favour a scenario where cluster ETGs experience environmental influence the longer they remain and the deeper into the gravitational potential they lie. Our findings indicate a combination of tidal stripping + harassment, which pre-dominate during infall, followed by mergers + feedback effects affecting ancient satellites and BCGs, respectively. The competition between tidal stripping and mergers is probably the key element for understanding the late evolution of ETGs toward their observed properties. At the same time, we should assume that these processes are superimposed on pre-processing mechanisms that may have happened in galaxy groups before infall. A more detailed study of this scenario is necessary, constituting a point to be further investigated in a future work.

ACKNOWLEDGEMENTS

We thank the anonymous referee for very helpful suggestions. ALBR thanks the support of CNPq grant 316317/2021-7 and FAPESB INFRA PIE 0013/2016. RSN thanks the financial support from CNPq grant 301132/2020-8. PAAL thanks the support of CNPq grants 433938/2018-8 e 312460/2021-0. CCD thanks the support by the Coordenação de Aperfeiçoamento de Pessoal de Nível Superior, Brasil (CAPES), Finance Code 001, the Programa Institucional de Internacionalização (PrInt—CAPES), and the Brazilian Space Agency (AEB) for the funding (PO 20VB.0009). MHSF thanks the financial support by the CAPES, Finance Code 001.

This research has made use of the SAO/NASA Astrophysics Data System, the NASA/IPAC Extragalactic Database (NED), and the ESA Sky tool (sky.esa.int/). Funding for the SDSS and SDSS-II was provided by the Alfred P. Sloan Foundation, the Participating Institutions, the National Science Foundation, the U.S. Department of Energy, the National Aeronautics and Space Administration, the Japanese Monbukagakusho, the Max Planck Society, and the Higher Education Funding Council for England. A list of participating institutions can be obtained from the SDSS website <http://www.sdss.org/>.

DATA AVAILABILITY

The data that support the findings of this study are available on request from the corresponding author, ALBR, upon reasonable request.

REFERENCES

- Adami C., Mazure A., Biviano A., Katgert P., Rhee G., 1998a, *A&A*, 331, 493
- Adami C., Mazure A., Katgert P., Biviano A., 1998b, *A&A*, 336, 63
- Aguado D. S. et al., 2019, *ApJS*, 240, 23
- Aguerri J. A. L., Sánchez-Janssen R., Muñoz-Tuñón C., 2007, *A&A*, 471, 17
- Alabi A. B. et al., 2017, *MNRAS*, 468, 3949
- Allen R. J. et al., 2015, *ApJ*, 806, 3
- Andreon S., 2018, *A&A*, 617, A53
- Ascaso B., Aguerri J., Varela J., Cava A., Bettoni D., Moles M., D’Onofrio M., 2010, *ApJ*, 726, 69
- Barchi P. et al., 2020, *Astron. Comput.*, 30, 100334
- Berlind A. A. et al., 2006, *ApJS*, 167, 1
- Bernardi M., 2009, *MNRAS*, 395, 1491
- Bernardi M. et al., 2003, *AJ*, 125, 1849
- Berrier J. C., Stewart K. R., Bullock J. S., Purcell C. W., Barton E. J., Wechsler R. H., 2008, *ApJ*, 690, 1292
- Binney J., Tremaine S., 1987, Princeton University Press, Princeton, NJ, 1987, 747
- Biviano A., Katgert P., Thomas T., Adami C., 2002, *A&A*, 387, 8
- Biviano A., Murante G., Borgani S., Diaferio A., Dolag K., Girardi M., 2006, *A&A*, 456, 23
- Blanton M. R., Moustakas J., 2009, *Annu. Rev. Astron. Astrophys.*, 47, 159
- Boselli A., Gavazzi G., 2006, *PASP*, 118, 517
- Buitrago F., Trujillo I., Curtis-Lake E., Montes M., Cooper A. P., Bruce V. A., Pérez-González P. G., Cirasuolo M., 2017, *MNRAS*, 466, 4888
- Cappellari M., 2016, *Annu. Rev. Astron. Astrophys.*, 54, 597
- Cappellari M. et al., 2006, *MNRAS*, 366, 1126
- Cava A. et al., 2017, *A&A*, 606, A108
- Chandrasekhar S., 1943, *ApJ*, 97, 255
- Cimatti A., Fraternali F., Nipoti C., 2019, *Introduction to Galaxy Formation and Evolution: From Primordial Gas to Present-Day Galaxies*. Cambridge University Press, Cambridge
- Coenda V., Rios M. d. I., Muriel H., Cora S. A., Martínez H. J., Ruiz A. N., Vega-Martínez C. A., 2022, *MNRAS*, 510, 1934
- Conover W. J., Iman R. L., 1979, Technical Report, Multiple-comparisons procedures. Informal report. Los Alamos National Lab.(LANL), Los Alamos, NM (United States)
- Conroy C., van Dokkum P. G., Kravtsov A., 2015, *ApJ*, 803, 77
- Cypriano E. S., Sodré L. Jr, Campusano L. E., Dale D. A., Hardy E., 2006, *AJ*, 131, 2417
- Daddi E. et al., 2005, *ApJ*, 626, 680
- Damjanov I. et al., 2009, *ApJ*, 695, 101
- Damjanov I. et al., 2011, *ApJ*, 739, L44
- Damjanov I., Zahid H. J., Geller M. J., Hwang H. S., 2015, *ApJ*, 815, 104
- De Propriis R., Bremer M. N., Phillipps S., 2016, *MNRAS*, 461, 4517
- de Carvalho R. R., Ribeiro A. L. B., Stalder D. H., Rosa R. R., Costa A. P., Moura T. C., 2017, *AJ*, 154, 96
- Di Cintio A., Tremmel M., Governato F., Pontzen A., Zavala J., Bastidas Fry A., Brooks A., Vogelsberger M., 2017, *MNRAS*, 469, 2845
- Di Matteo P., Pipino A., Lehnert M. D., Combes F., Semelin B., 2009, *A&A*, 499, 427
- Domínguez Sánchez H., Huertas-Company M., Bernardi M., Tuccillo D., Fischer J. L., 2018, *MNRAS*, 476, 3661
- Dressler A., Shectman S. A., 1988, *AJ*, 95, 985
- Edwards L. O., Patton D. R., 2012, *MNRAS*, 425, 287
- Evrard A. E. et al., 2008, *ApJ*, 672, 122
- Faber S. M., Jackson R. E., 1976, *ApJ*, 204, 668
- Fadda D., Girardi M., Giuricin G., Mardirossian F., Mezzetti M., 1996, *ApJ*, 473, 670
- Feldmann R., Carollo C. M., Mayer L., 2011, *ApJ*, 736, 88
- Gargiulo A., Saracco P., Longhetti M., La Barbera F., Tamburri S., 2012, *MNRAS*, 425, 2698
- Gill S. P., Knebe A., Gibson B. K., 2005, *MNRAS*, 356, 1327
- Girardi M., Giuricin G., Mardirossian F., Mezzetti M., Boschin W., 1998, *ApJ*, 505, 74
- Goto T., 2005, *MNRAS*, 359, 1415

- Graves G. J., Faber S., Schiavon R. P., 2009, *ApJ*, 693, 486
- Guo Q., White S., Li C., Boylan-Kolchin M., 2010, *MNRAS*, 404, 1111
- Hilz M., Naab T., Ostriker J. P., 2013, *MNRAS*, 429, 2924
- Huang Y.-H., Chen H.-W., Johnson S. D., Weiner B. J., 2016, *MNRAS*, 455, 1713
- Hyde J. B., Bernardi M., 2009, *MNRAS*, 396, 1171
- Iodice E. et al., 2017, *ApJ*, 839, 21
- Johansson P. H., Naab T., Ostriker J. P., 2012, *ApJ*, 754, 115
- Joshi G. D., Wadsley J., Parker L. C., 2017, *MNRAS*, 468, 4625
- Kauffmann G., White S. D. M., Heckman T. M., Ménard B., Brinchmann J., Charlot S., Tremonti C., Brinkmann J., 2004, *MNRAS*, 353, 713
- Kuchner U. et al., 2022, *MNRAS*, 510, 581
- La Barbera F., De Carvalho R., 2009, *ApJ*, 699, L76
- La Barbera F., Lopes P. A. A., de Carvalho R. R., de La Rosa I. G., Berlind A. A., 2010, *MNRAS*, 408, 1361
- Lani C. et al., 2013, *MNRAS*, 435, 207
- Lintott C. J. et al., 2008, *MNRAS*, 389, 1179
- Liu F., Mao S., Deng Z., Xia X., Wen Z., 2009, *MNRAS*, 396, 2003
- Liu F., Lei F., Meng X., Jiang D., 2015, *MNRAS*, 447, 1491
- Łokas E. L., 2020, *A&A*, 638, A133
- Lopes P. A. A., 2007, *MNRAS*, 380, 1608
- Lopes P. A. A., de Carvalho R. R., Kohl-Moreira J. L., Jones C., 2009, *MNRAS*, 392, 135
- López-Sanjuan C. et al., 2012, *A&A*, 548, A7
- Mamon G., Cava A., Biviano A., Moretti A., Poggianti B., Bettoni D., 2019, *A&A*, 631, A131
- Mancillas B., Duc P.-A., Combes F., Bournaud F., Emsellem E., Martig M., Michel-Dansac L., 2019, *A&A*, 632, A122
- Matharu J. et al., 2019, *MNRAS*, 484, 595
- Matteuzzi M., Marinacci F., Nipoti C., Andreon S., 2022, *MNRAS*, 513, 3893
- McIntosh D. H., Guo Y., Hertzberg J., Katz N., Mo H., Van Den Bosch F. C., Yang X., 2008, *MNRAS*, 388, 1537
- Miller T. B., van den Bosch F. C., Green S. B., Ogiya G., 2020, *MNRAS*, 495, 4496
- Morell D., Ribeiro A., de Carvalho R., Rembold S., Lopes P., Costa A., 2020, *MNRAS*, 494, 3317
- Muriel H., Coenda V., 2014, *A&A*, 564, A85
- Naab T., Johansson P. H., Ostriker J. P., 2009, *ApJ*, 699, L178
- Nair P. B., Abraham R. G., 2010, *ApJS*, 186, 427
- Nascimento R. S., Lopes P. A., Ribeiro A. L., Costa A. P., Morell D. F., 2019, *MNRAS*, 483, L121
- Newman A. B., Ellis R. S., Treu T., Bundy K., 2010, *ApJ*, 717, L103
- Nigoche-Netro A., Ramos-Larios G., Lagos P., De la Fuente E., Ruelas-Mayorga A., Mendez-Abreu J., Kemp S., Diaz R., 2019, *MNRAS*, 488, 1320
- Nipoti C., 2017, *MNRAS*, 467, 661
- Old L. et al., 2015, *MNRAS*, 449, 1897
- Oogi T., Habe A., Ishiyama T., 2016, *MNRAS*, 456, 300
- Oser L., Ostriker J. P., Naab T., Johansson P. H., Burkert A., 2010, *ApJ*, 725, 2312
- Ownsworth J. R., Conselice C. J., Mortlock A., Hartley W. G., Almaini O., Duncan K., Mundy C. J., 2014, *MNRAS*, 445, 2198
- Park C., Choi Y.-Y., 2005, *ApJ*, 635, L29
- Pasquali A., Smith R., Gallazzi A., De Lucia G., Zibetti S., Hirschmann M., Yi S. K., 2019, *MNRAS*, 484, 1702
- Peletier R. F., Davies R. L., Illingworth G. D., Davis L. E., Cawson M., 1990, *AJ*, 100, 1091
- Peng Y.-j. et al., 2010, *ApJ*, 721, 193
- Pillepich A. et al., 2018, *MNRAS*, 475, 648
- Popesso P., Biviano A., Böhringer H., Romaniello M., Voges W., 2005, *A&A*, 433, 431
- Popesso P., Biviano A., Böhringer H., Romaniello M., 2007, *A&A*, 464, 451
- Poveda A., 1958, *Bol. Obs. Tonantzintla Tacubaya*, 2, 3
- Rasmussen J., Mulchaey J. S., Bai L., Ponman T. J., Raychaudhury S., Dariush A., 2010, *ApJ*, 717, 958
- Renzini A., 2006, *Annu. Rev. Astron. Astrophys.*, 44, 141
- Rhee J., Smith R., Choi H., Yi S. K., Jaffé Y., Candlish G., Sánchez-Jánsssen R., 2017, *ApJ*, 843, 128
- Rhee J., Smith R., Choi H., Contini E., Jung S. L., Han S., Suhyoung K. Y., 2020, *ApJS*, 247, 45
- Ribeiro A. L. B., de Carvalho R. R., Trevisan M., Capelato H. V., La Barbera F., Lopes P. A. A., Schilling A. C., 2013, *MNRAS*, 434, 784
- de los Rios M., Martínez H. J., Coenda V., Muriel H., Ruiz A. N., Vega-Martínez C. A., Cora S. A., 2021, *MNRAS*, 500, 1784
- Rocha M., Peter A. H., Bullock J. S., Kaplinghat M., Garrison-Kimmel S., Onorbe J., Moustakas L. A., 2013, *MNRAS*, 430, 81
- Rodríguez-Gomez V. et al., 2016, *MNRAS*, 458, 2371
- Roy N. et al., 2018, *MNRAS*, 480, 1057
- Sampaio V., de Carvalho R., Ferreras I., Laganá T., Ribeiro A., Rembold S., 2021, *MNRAS*, 503, 3065
- Saracco P., Gargiulo A., Ciocca F., Marchesini D., 2017, *A&A*, 597, A122
- Schechter P. L., 2016, in Bragaglia A., Arnaboldi M., Rejkuba M., Romano D., eds, *The General Assembly of Galaxy Halos: Structure, Origin and Evolution*. Vol. 317, Cambridge University Press, p. 35
- Shankar F., Marulli F., Bernardi M., Mei S., Meert A., Vikram V., 2013, *MNRAS*, 428, 109
- Shen S., Mo H., White S. D., Blanton M. R., Kauffmann G., Voges W., Brinkmann J., Csabai I., 2003, *MNRAS*, 343, 978
- Signorell A. et al., 2016, *R Foundation for Statistical Computing*, Vienna, Austria
- Simard L., Mendel J. T., Patton D. R., Ellison S. L., McConnachie A. W., 2011, *ApJS*, 196, 11
- Smith R., Choi H., Lee J., Rhee J., Sanchez-Janssen R., Suhyoung K. Y., 2016, *ApJ*, 833, 109
- Sodre L. Jr, Capelato H. V., Steiner J. E., Mazure A., 1989, *AJ*, 97, 1279
- Song H., Hwang H. S., Park C., Smith R., Einasto M., 2018, *ApJ*, 869, 124
- Stein P., Jerjen H., Federspiel M., 1997, *A&A*, 327, 952
- Tamfal T., Mayer L., Quinn T. R., Capelo P. R., Kazantzidis S., Babul A., Potter D., 2021, *ApJ*, 916, 55
- Thomas D., Maraston C., Bender R., De Oliveira C. M., 2005, *ApJ*, 621, 673
- Tortora C., Napolitano N., 2022, *Front. Astron. Space Sci.*, 8, 197
- Tortora C., Napolitano N. R., Roy N., Radovich M., Getman F., Koopmans L., Verdoes Kleijn G., Kuijken K., 2018, *MNRAS*, 473, 969
- Tran K.-V. H., Moustakas J., Gonzalez A. H., Bai L., Zaritsky D., Kautsch S. J., 2008, *ApJ*, 683, L17
- Trujillo I., Conselice C. J., Bundy K., Cooper M., Eisenhardt P., Ellis R. S., 2007, *MNRAS*, 382, 109
- Trujillo I., Ferreras I., de La Rosa I. G., 2011, *MNRAS*, 415, 3903
- Van Dokkum P. G., Conroy C., 2010, *Nature*, 468, 94021124316
- Van Dokkum P. G. et al., 2008, *ApJ*, 677, L5
- van der Wel A. et al., 2014, *ApJ*, 788, 28
- Wellons S., Torrey P., 2017, *MNRAS*, 467, 3887
- Whitaker K. E., Kriek M., Van Dokkum P. G., Bezanson R., Brammer G., Franx M., Labbé I., 2012, *ApJ*, 745, 179
- Willett K. W. et al., 2013, *MNRAS*, 435, 2835
- Yang X., Mo H., Van den Bosch F. C., Pasquali A., Li C., Barden M., 2007, *ApJ*, 671, 153
- Yoon Y., Park C., 2020, *ApJ*, 897, 121
- Yoon Y., Im M., Kim J.-W., 2017, *ApJ*, 834, 73
- Zahid H. J., Geller M. J., Fabricant D. G., Hwang H. S., 2016, *ApJ*, 832, 203
- Zahid H. J., Sohn J., Geller M. J., 2018, *ApJ*, 859, 96

APPENDIX A: ESTIMATING THE EFFECT OF CONTAMINANTS IN PPS REGIONS

In this appendix, we present a brief analysis on projection effects to determine whether potential misclassifications of data points in the four regions of the PPS could lead to significant changes in the trends found for the corresponding observables. The idea is to trace such effects as clearly as possible, hence we focus on a very simple model subjected to a well-controlled bootstrap test.

We constructed a synthetic data set with 1000 randomly generated points on the PPS (Fig. A1, left-hand panel), with coordinates within $0 < R/R_{200} < 3$ and $0 < \Delta V/\sigma < 3$, taken from a 2D Gaussian

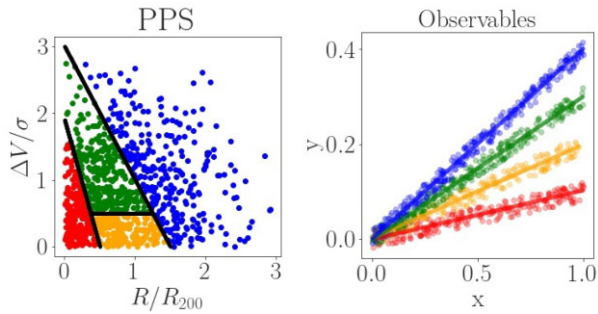


Figure A1. Synthetic data set with 1000 points. *Left:* PPS generated from a 2D Gaussian distribution; *right:* observable trends based on a linear model.

distribution with mean (0.01, 0.01) and unit covariance matrix. For the synthetic observable y (Fig. A1, right-hand panel), we constructed linear trends, $y = ax$, with different slopes for each PPS class, randomly choosing both the x coordinate (from 0 to 1), as well

as the spread around the linear correlation ($0 < |\Delta y| < 0.02$). The slopes were $a = \{0.1, 0.2, 0.3, 0.4\}$ for the classes $\mathcal{C} = \{ \text{'ancient'}, \text{'intermediate'}, \text{'recent'}, \text{'first infallers'} \}$, respectively.

We assumed the same contamination fractions in each region of the PPS as given by Rhee et al. (2017; cf. their fig. 6). For each reference class, we randomly selected points from the other three regions, according to the contamination fractions for this class, and reclassified the selected data points to the given reference class.

In Fig. A2 (first row of panels), we illustrate this procedure on the PPS, where the reclassified (or ‘moved’) data points are highlighted and signalled with a cross. In Fig. A2 (second row of panels), we show the corresponding (reclassified) data points in the observable space. So, for each class, we reclassified galaxies that were contaminating the other classes, moving them to the given class in question. Hence, we see how the correlations of the observables change statistically. The above procedure was independently repeated 100 times. In Fig. A2 (third row of panels), we present for each reference class a linear regression fit to the binned data points generated by this bootstrap procedure. We also show the original correlations for

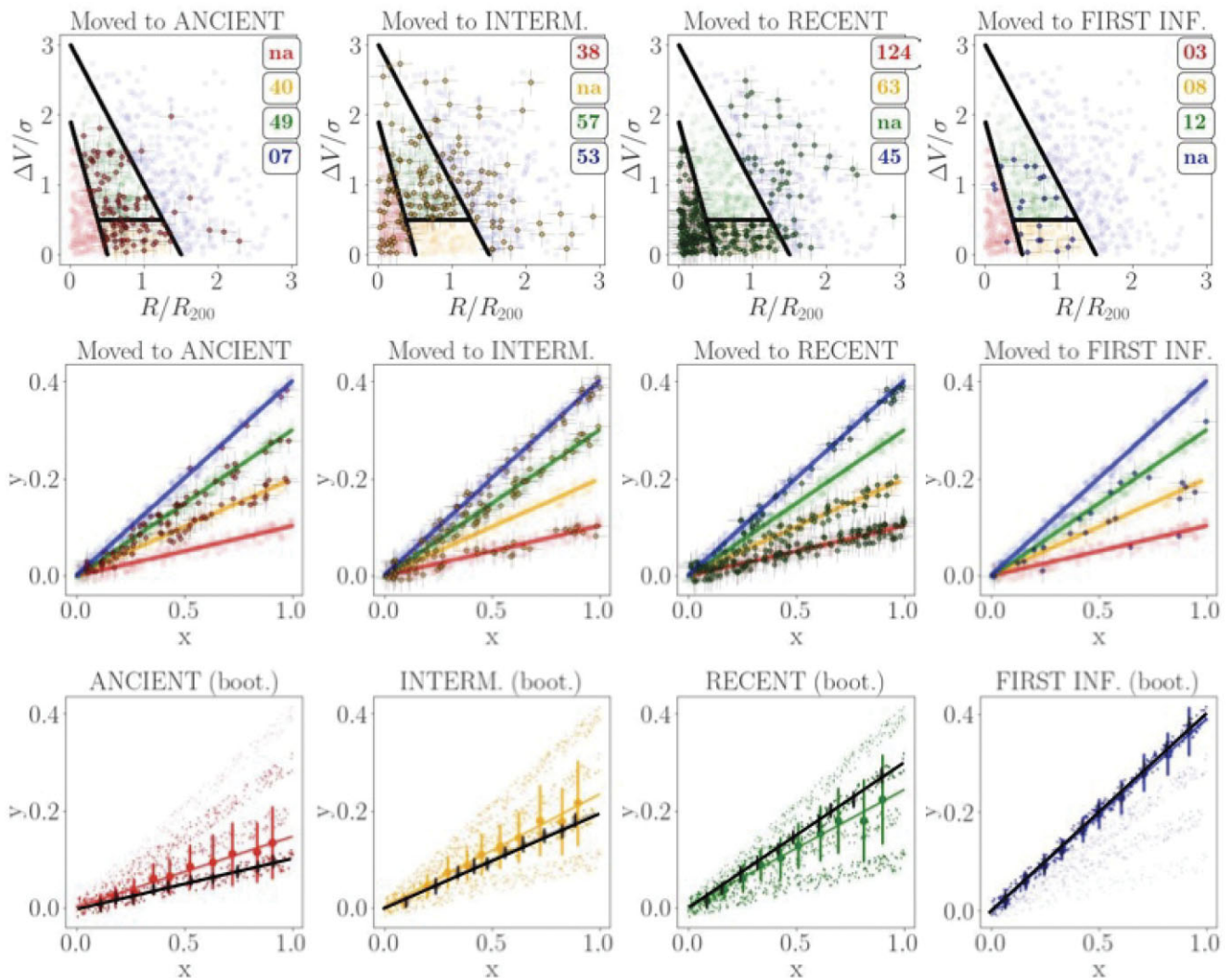


Figure A2. Bootstrap analysis. *First row of panels:* the reclassified (or ‘moved’) data points, highlighted and signalled with a cross. The number of reclassified data points for each class is shown in the legend (‘na’ means not applicable). *Second row of panels:* the corresponding (reclassified) data points in the observable space. *Third row of panels:* a linear regression fit to the binned data points generated by the bootstrap procedure. Vertical bars indicate the standard deviation of the observations in each bin. We also show the original correlations for comparison (in black).

comparison. We found that the impact of contamination is larger for the ranges in x where the correlations of the observables differ more among classes (namely, as $x \rightarrow 1$). The ‘first infallers’ show almost no changes due to the very small contamination fractions for this class.

It can also be observed in Fig. A2 (first row of panels) that the overall highest numbers of misclassified data points (i.e. points that needed to be moved from other classes into a given reference class) were obtained for the ‘recent’ class. This means there could be a non-negligible observational contamination of the latter class into the other classes, especially into the ‘ancient’ class (i.e. 124 data points were moved out from this class). Next in misclassification significance is the ‘intermediate’ class, which required moving data points from the ‘recent’ class (57 data points) and from the ‘first infallers’ (53) class. Next, the ‘ancient’ class received data points from the ‘recent’ class (49) and the ‘intermediate’ (40) class. The resulting effective contaminations can be evaluated by a comparison between the respective original correlations (black colour) and those obtained after reclassifying the data points into their correct classes (cf. the third row of panels in Fig. A2).

From this simple test, we obtained a qualitative gauge for the contamination effects. It was also possible to roughly predict the

direction along the y -axis as a given class would change if misclassifications were accounted for. For instance, the observable trend of the ‘ancient’ class (Fig. A2) moved upwards in y , and this is clearly because the trends of the other classes (with some misclassified ‘ancients’) had higher slopes. When these misclassified ‘ancients’ were corrected in the bootstrap, the tendency was to produce an ‘ancient’ correlation with a higher slope. This can be similarly observed for the ‘intermediate’ (upward shift) and ‘recent’ classes (downward shift).

We conclude with the following hints: (1) within some interval in Δx , a given class would probably move upwards (downwards) in y depending on the corresponding values of the other classes having higher (lower) values in $y(\Delta x)$; and (2) as long as the observable correlations do not diverge too much among each other (roughly, within their confidence intervals), the unavoidable misclassifications of classes based on the PPS should not lead to significant changes in the trends, at least based on the contamination fractions here adopted.

This paper has been typeset from a $\text{\TeX}/\text{\LaTeX}$ file prepared by the author.